

See discussions, stats, and author profiles for this publication at: <https://www.researchgate.net/publication/236943899>

Chemical Dynamics Study of NO Scattering from a Perfluorinated Self-Assembled Mono layer

ARTICLE *in* THE JOURNAL OF PHYSICAL CHEMISTRY C · DECEMBER 2011

Impact Factor: 4.77 · DOI: 10.1021/jp206034c

CITATIONS

11

READS

40

4 AUTHORS:



Juan J. Nogueira

University of Vienna

15 PUBLICATIONS 81 CITATIONS

[SEE PROFILE](#)



Zahra Homayoon

Emory University

18 PUBLICATIONS 98 CITATIONS

[SEE PROFILE](#)



Saulo A Vázquez

University of Santiago de Compostela

90 PUBLICATIONS 1,045 CITATIONS

[SEE PROFILE](#)



Emilio Martinez-Nuñez

University of Santiago de Compostela

85 PUBLICATIONS 1,019 CITATIONS

[SEE PROFILE](#)

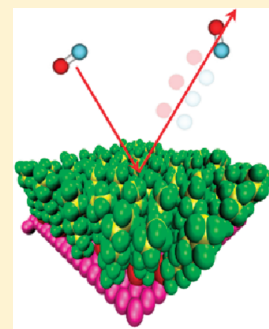
Chemical Dynamics Study of NO Scattering from a Perfluorinated Self-Assembled Monolayer

Juan J. Nogueira, Zahra Homayoon,[†] Saulo A. Vázquez,* and Emilio Martínez-Núñez*

Departamento de Química Física and Centro Singular de Investigación en Química Biológica y Materiales Moleculares, Campus Vida, Universidad de Santiago de Compostela, 15782 Santiago de Compostela, Spain

 Supporting Information

ABSTRACT: In this paper, the dynamics of NO scattering off a perfluorinated self-assembled monolayer was studied by means of chemical dynamics simulations. An analytical function was developed for the interaction between the projectile and the surface, based on focal point-CCSD(T)/CBS ab initio results. The trajectories that perform a minimum number of moderate changes in the direction of the rotational angular momentum J provide thermal accommodation of the rotational degrees of freedom, whereas those that suffer abrupt changes in J do not thermalize rotation. This analysis provides better thermalization coefficients than previous analysis based on changes in the direction of the velocity vector of the projectile in the perpendicular direction. An energy transfer model is presented that fits very well the simulation results. Analysis of the stereodynamics of the scattered projectiles indicates that there is a preference for corkscrew and cartwheel topspin rotational motions. The simulation results agree very well with previous experimental data on NO scattering off a similar surface.



I. INTRODUCTION

Considerable interest has been placed in the last two decades on the study of energy transfer in collisions of gas-phase species with self-assembled monolayers (SAMs)^{1–34} and with liquid surfaces.^{35–46} One of the signatures of the scattering mechanism is the final translational energy distribution of the projectile $P(E_f)$. Depending on the initial conditions and the particular system under study, the $P(E_f)$ distributions can be fit with a single Boltzmann distribution and can also be bimodal or exhibit a more complicated shape. A simple gas–surface interaction model, which identifies each component of the distribution with a particular gas–surface interaction mechanism, has been used in many previous studies. In particular, the low-energy component of the $P(E_f)$ distributions, which is, many times, well fit by a Boltzmann distribution at T_s , is associated with a thermal desorption (TD) mechanism,⁴⁷ in which the projectile physisorbs or penetrates into the bulk of the liquid (or surface) reaching thermal accommodation. By contrast, according to this model the high-energy component (sometimes fitted to a Boltzmann distribution with a temperature higher than T_s) arises from an impulsive scattering (IS) mechanism, where the projectile immediately rebounds from the surface in such a short time scale that thermal equilibration with the surface does not take place.

Recent chemical dynamics simulations of gas-phase species scattering off SAM surfaces indicate that the scattering process may be considerably more complex. It was found that direct events, without trapping on the surface, may contribute to the low-energy component, and on the other hand, trajectories that physisorb or penetrate inside the monolayers may contribute to

the high-energy component.^{5,9,17,20,48} In particular, in a recent $\text{CO}_2 + \text{a perfluorinated SAM}$ (or F-SAM) dynamics study, the percentage of penetrating and physisorption events did not match the relative contribution of the low-energy component of the $P(E_f)$ distribution, i.e., TD cannot be unambiguously identified with the low-energy component of the $P(E_f)$ distribution.⁵ Furthermore, the distributions of the rotational quantum numbers of the scattered CO_2 molecules $P(J)$ are also bimodal, but the relative contribution of each component differs from those obtained for $P(E_f)$.⁵

An interesting aspect of the gas–surface dynamics is the energy transfer efficiencies to the various degrees of freedom of the molecule and to the surface. Previous simulation results of projectile ions + surface collisions show that the percentage (with respect to the collision energy) of energy transfer to the projectile's internal degrees of freedom does not depend much on the collision energy, while energy transfer to the surface increases.^{7,31,49,50} A model proposed previously⁷ shows that the function $\exp(-b/E_i)$ fits reasonably well the average percentage energy transfer to the surface as a function of the collision energy E_i . This model predicts that the high E_i limiting energy transfer to the surface is ~90% for two protonated peptides scattering off an F-SAM.⁷ The same model was employed by Morris and co-workers to obtain values for the high E_i limiting energy transfer to the surface of 89–98% for Ar and CO_2 scattering off several SAM surfaces.³⁴

One of the projectiles that has attracted much attention in recent years is CO_2 . The collision dynamics of CO_2 with F-SAM

[†] On leave from the Department of Chemistry, College of Sciences, Shiraz University, Shiraz 71454, Iran.

Received: June 27, 2011

Revised: September 27, 2011

Published: October 27, 2011

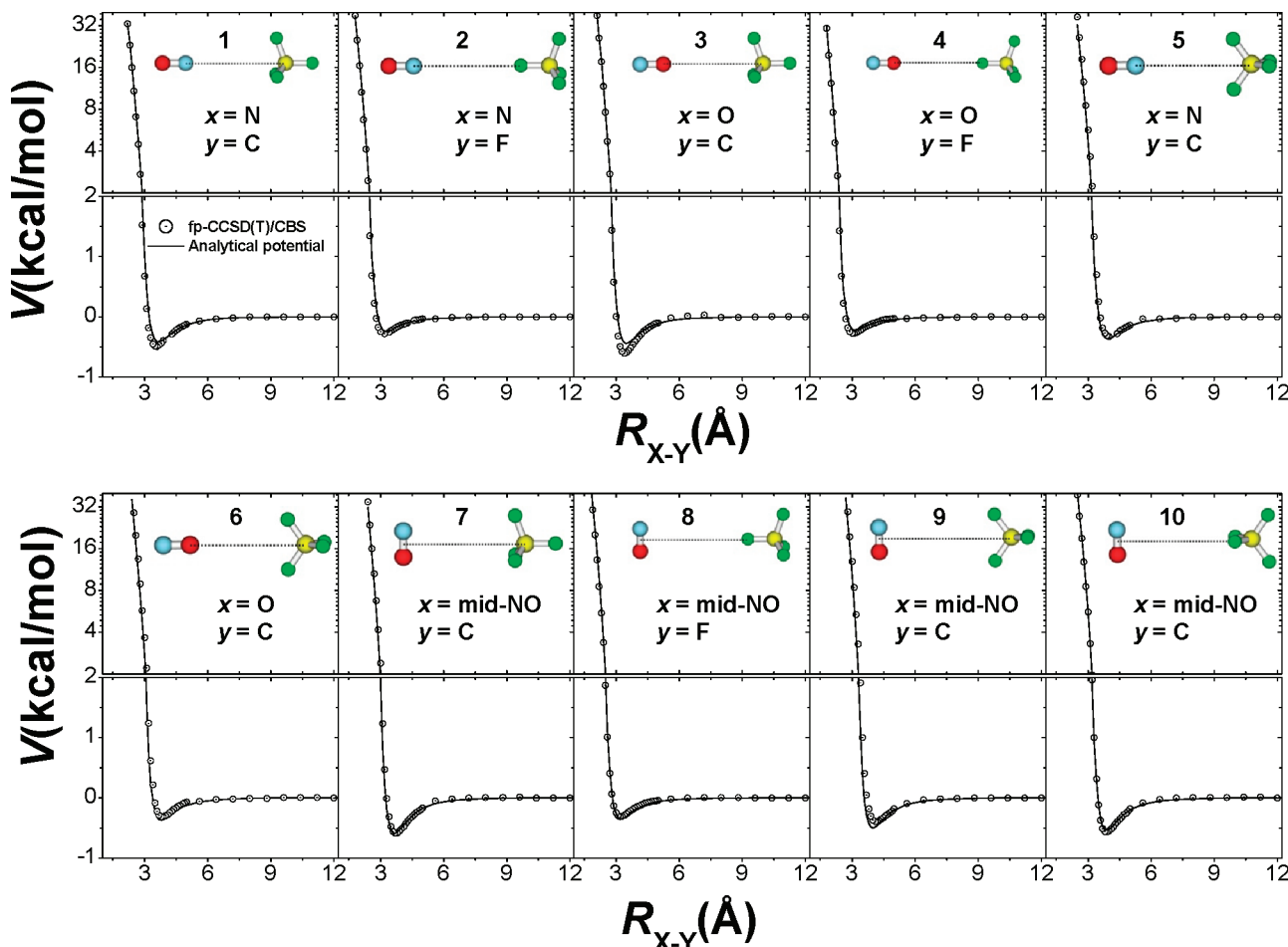


Figure 1. Analytical potential of eq 4 fitted to the fp-CCSD(T)/CBS ab initio calculations for the 10 different orientations of the NO + CF₄ system considered in this study to develop the NO + F-SAM interaction potential.

or similar surfaces has been studied by Nesbitt's group^{35–43} and our own group in collaboration with Hase's group.^{4,5,9} Nesbitt's group analyzed in detail the influence of the incident angle, collision energy, and surface temperature on the scattering dynamics. Also, the stereodynamics was studied in much detail.^{39,43} Quite interestingly, they found that CO₂ scatters off the surface in a helicopter fashion for $J < 60$, whereas for the higher rotational states the molecule exhibits cartwheel rotational motion. On the other hand, Troya and co-workers found that cartwheel rotational motion is the preferred behavior for CO scattering off an F-SAM.³³ For both systems CO₂ + FSAM and CO + F-SAM, cartwheel motion has the same orientation of J, i.e., with forward (or topspin) sense of end-over-end tumbling.

In the present paper the collision dynamics of NO + F-SAM is studied by means of chemical dynamics simulations. As mentioned above, previous simulation results show that TD and IS are more complex mechanisms that cannot be rationalized in terms of different trajectory types. In the present paper a new scheme to sort the trajectories is presented, based on the assumption that thermal accommodation of the rotational degrees of freedom takes place after NO suffers a sufficiently large number of gentle "kicks" that produce deviations of the angular momentum vector.

Additionally, a new model of gas–surface energy transfer is presented here. The model is based on the adiabaticity parameter⁵¹

and fits very accurately the NO + F-SAM simulation results. The stereodynamics of the NO + F-SAM collision dynamics is also studied in detail and compared with previous results on CO₂ + F-SAM⁴³ and CO + F-SAM.³³

Finally, the pioneering work of Cohen et al. on the collision dynamics of He, Ar, O₂, and NO + SAM surfaces^{1,2} also motivated the present study. Among the SAMs employed in their studies, they used perfluorinated acid ester (PFAE). This monolayer is entirely fluorinated over the outer eight carbons of the chain, exposing the –CF₃ groups, being therefore very similar to the F-SAM employed in our previous gas–surface simulations^{3–9} and in the present study. Therefore, a direct comparison of the experimental and simulation results is possible, which serves to test the theoretical methods.

II. COMPUTATIONAL DETAILS

II.A. Potential Energy Surface. The potential energy function of the system consists of the F-SAM intramolecular interaction V_{surf} , the NO intramolecular interaction V_{NO} , and the interaction between NO and the surface $V_{\text{NO-surf}}$

$$V = V_{\text{surf}} + V_{\text{NO}} + V_{\text{NO-surf}} \quad (1)$$

The intramolecular potential function for the F-SAM surface V_{surf} was explained in detail elsewhere.^{8,9} The monolayer consists

of 48 chains of $\text{CF}_3(\text{CF}_2)_7\text{S}$ radicals adsorbed on a single layer of 225 Au atoms, which are kept fixed during the dynamics simulations. An all-atom (AA) model was utilized, where every single atom constitutes an interaction site. This AA model is able to reproduce the 300 K structure of the surface, i.e., the monolayer forms a hexagonal close-packed structure with the nearest-neighbor direction rotated 30° with respect to the Au-{111} lattice, and the backbone of the $\text{CF}_3(\text{CF}_2)_7\text{S}$ moiety has a tilt angle with respect to the surface normal of ~12°.⁹

The NO intramolecular interaction energy contains only one term. For most of the simulations a simple harmonic potential $V_{\text{NO}}^{\text{harm}}$ was employed. In one simulation that involves collisions of highly vibrationally excited NO molecules with the F-SAM (see section II.B) the NO stretching interaction was modeled using a Morse expression $V_{\text{NO}}^{\text{Morse}}$

$$\begin{aligned} V_{\text{NO}}^{\text{harm}} &= \frac{k_s}{2} (r_0 - r)^2 \\ V_{\text{NO}}^{\text{morse}} &= D_e \{1 - \exp[-\beta(r - r_0)]\}^2 \end{aligned} \quad (2)$$

where the force constant k_s is obtained from the harmonic oscillator relationship $k_s = 4\pi^2 c^2 \mu \tilde{v}^2$, $\beta = (2\pi^2 c^2 \mu \tilde{v}^2 / D_e)^{1/2}$, c is the speed of light, μ is the reduced mass, D_e is the dissociation energy, and \tilde{v} is the vibrational frequency of the diatomic molecule (in wavenumbers). The CCSD(T)/aug-cc-pVDZ stretching frequency \tilde{v} (scaled by 0.982) of 1978 cm⁻¹ and equilibrium distance r_0 of 1.164 Å were employed. Finally, for the dissociation energy the experimental value 152.54 kcal/mol⁵² was used.

In order to calculate the NO/F-SAM interaction potential $V_{\text{NO-surf}}$ a potential energy function was computed for the NO + CF_4 system, following the strategy of previous studies,^{3,8,9,53–55} where the carbon and fluorine atoms of CF_4 were regarded as representative of those in the F-SAM. The gas–surface interaction energies that this approach provides agree very well with those obtained using more realistic models for the F-SAM surface.³ Due to the open-shell character of nitric oxide, the electronic degeneracy of its ground ($X^2\Pi$) electronic state is split when it interacts with the CF_4 molecule.⁵⁶ The resulting Λ -doublet levels (A' and A'' in C_s symmetry) are computed in this work at the UCCSD(T)/aug-cc-pVDZ level of theory⁵⁷ using MOLPRO⁵⁸ (see Figure 1 of the Supporting Information). Since the goal of this part of the study is to investigate the splitting of the Λ -doublet levels rather than obtaining accurate energy values, the results are not corrected for basis-set superposition error. Previous quasi-classical trajectory calculations on the related NO + Ar system employed an average potential for the dynamics $V_{\text{sum}} = 1/2(V_{A'} + V_{A''})$.⁵⁹ The difference between $V_{A'}$ and V_{sum} obtained in our calculations is, on average, 0.03 kcal/mol at the minima, and the root-mean-square difference between the $V_{A'}$ and the V_{sum} curves is 0.82 kcal/mol. Moreover, the position of the minima does not change much in both $V_{A'}$ and V_{sum} surfaces. Important differences between both doublet levels were found, however, for NO($X^2\Pi$) interacting with Ag(111).⁵⁶

The splitting of the Λ -doublet levels for NO($X^2\Pi$) + CF_4 is small and probably of the order of the combined error of the ab initio calculations and the fit of the potential energy function (vide infra). On the other hand, the focus of our paper is not on a detailed comparison with experiment. Therefore, the NO/F-SAM interaction potential was developed using only the $V_{A'}$ potential energy surface.

Table 1. Parameters of the $\text{NO} \cdots \text{CF}_4$ Intermolecular Analytical Potential of eq 4^a

$i-j$	A_{ij}	B_{ij}	C_{ij}	D_{ij}	E_{ij}	F_{ij}
N–C	1222.363	2.486				
N–F	96 826.251	4.000	99.622	5.200	5904.001	9.000
O–C	17 873.835	3.594			90.262	8.997
O–F	114 690.455	4.270	46.833	5.000	3540.142	9.000

^a Units are such that potential energy is in kcal/mol and distance is Angstroms.

More accurate NO + CF_4 interaction energies of A' symmetry can be computed as detailed below. For the 10 orientations between the NO and the CF_4 molecules of Figure 1, MP2/aug-cc-pVXZ (X = D,T,Q) and CCSD(T)/aug-cc-pVDZ single-point energies were computed using Gaussian09.⁶⁰ The ab initio calculations include the counterpoise correction to account for the basis-set superposition error (BSSE). Additionally, the MP2/aug-cc-pVXZ values were extrapolated to the complete basis-set limit (CBS) using Peterson's prescription⁶¹

$$E(n) = E_{\text{CBS}} + A \exp[-(n + 1)] + B \exp[-(n + 1)^2] \quad (3)$$

with $n = 2, 3$, and 4 for X = D, T, and Q, respectively, and $E(n)$ represents the MP2/aug-cc-pVXZ energy. In order to obtain more accurate energies, the focal-point approximation of Allen and co-workers⁶² has been employed in this study. The method takes advantage of the fact that, usually, for large basis sets the difference between the MP2 and the CCSD(T) energies is independent of the basis set. In this work, CCSD(T) energies at the CBS limit (here and after fp-CCSD(T)/CBS) were computed with the focal point approach.

The analytical function employed to fit to the fp-CCSD(T)/CBS interaction energies is a sum of two-body Buckingham potentials

$$V_{\text{NO-surf}} = \sum_{ij} A_{ij} \exp(-B_{ij}R_{ij}) - C_{ij}/R_{ij}^{D_{ij}} - E_{ij}/R_{ij}^{F_{ij}} \quad (4)$$

where i and j represent each of the atoms of the NO and CF_4 molecules, respectively, R_{ij} is the $i-j$ interatomic distance, and $A_{ij}, B_{ij}, \dots, F_{ij}$ are the parameters. The fit was conducted with the help of a generic algorithm.⁶³

Figure 1 shows the results of the fit (solid line) for the 10 NO \cdots CF_4 orientations chosen in this study, and the final two-body parameters are collected in Table 1. The root-mean-square error of the fit is 4×10^{-2} kcal/mol.

To prevent NO molecules from unphysical penetration through the gold surface, N–Au and O–Au potential functions were added. In the absence of accurate potential functions and following previous work,^{9,64} the repulsive parts of the N–C and O–C two-body potentials of eq 4 were employed for N–Au and O–Au, respectively.

II.B. Chemical Dynamics Simulations. Ten different initial conditions (ICs) were considered for the simulations. The ICs differ from each other in the initial collision energy of the projectile E_p , the incident angle θ_i formed between the incident velocity and the surface normal, and the initial ro-vibrational state (v, J) of the NO molecule, where v and J are the NO vibrational and rotational quantum numbers, respectively. Details of each IC are collected in Table 2. When $\theta_i > 0$, an azimuthal angle χ is

Table 2. Different Initial Conditions ICs Considered in This Work for the Simulations

IC	N_{traj}^a	E_i^b	θ_i	$(v_J)^c$
1	6×10^3	1.0	0	(0, 6 K)
2	6×10^3	3.2	0	(0, 6 K)
3	6×10^3	4.6	0	(0, 6 K)
4	6×10^3	6.7	0	(0, 6 K)
5	6×10^3	10.6	0	(0, 6 K)
6	6×10^3	40.0	0	(0, 6 K)
7	6×10^3	10.6	0	(15, 0)
8	10^4	10.6	30	(0, 0)
9	10^4	10.6	30	(0, 30)
10	10^4	10.6	60	(0, 0)

^a Number of trajectories. ^b In kcal/mol. ^c 6 K means that J was taken from a 6 K Boltzmann distribution of rotational states.

defined as the projection of the velocity vector onto the surface plane. This angle χ was randomly selected between 0 and 2π .

ICs 2–5 were selected to mimic the experimental conditions employed by Cohen et al. in their study of NO scattering off a perfluorinated acid ester (PFAE) monolayer.^{1,2} The rotational excitation of nitric oxide was taken from a Boltzmann distribution at 6 K, which accounts for 94% of the total experimental $P(J)$ distribution, as seen in Figure 2 of the Supporting Information.

The surface used in our simulations, F-SAM, consists of $\text{CF}_3(\text{CF}_2)_7\text{S}$ chains supported on $\text{Au}\{111\}$. The one employed in the experiments, PFAE, was prepared by self-assembling $\text{CF}_3(\text{CF}_2)_9-(\text{CH}_2)_2\text{OCO}(\text{CH}_2)_8\text{COOH}$ chains on glass.² Both surfaces are structurally similar, particularly the upper part of the monolayer. Previous work in our group, on the scattering dynamics of $\text{CO}_2 + \text{F-SAM}$,⁵ suggests that energy transfer between the projectile and the surface is essentially controlled by the outermost layer of the surface (the $-\text{CF}_3$ groups) and not by the detailed structure of the interfacial material, which renders support for the comparison made here. Other research groups also observed similar energy transfer efficiencies to different surfaces with terminal $-\text{CF}_3$ groups.⁶⁵

ICs 1 and 6 were devised to investigate energy transfer efficiencies in a larger energy range. Additionally, different ro-vibrational states of the projectile were investigated in ICs 7 and 9 as well as different incident angles (ICs 8–10).

All simulations of the present study have been carried out using the VENUS05⁶⁶ computer program. Ensembles of trajectories corresponding to the ICs of Table 2 were integrated with a fixed step size of 0.3 fs using the Adams–Moulton algorithm in VENUS05 for a total integration time of 90 ps. Before the beginning of each trajectory simulation the surface was relaxed to a thermodynamic equilibrium structure by a 2 ps molecular dynamics simulation⁶⁷ in which the atomic velocities are scaled to obtain a surface temperature of 300 K. This structure was then used as the initial structure of a 100 fs equilibration run at the beginning of each trajectory. Periodic boundary conditions were also utilized to simulate a larger surface.⁶⁷ After integration of each trajectory, the surface energy, translational and internal energies, rotational angular momentum, orientation, and velocity of the scattered NO molecule were calculated from the atomic Cartesian coordinates and momenta.

III. RESULTS AND DISCUSSION

III.A. Collision Types.

Three collision types were found in our simulations. The different events were identified according to

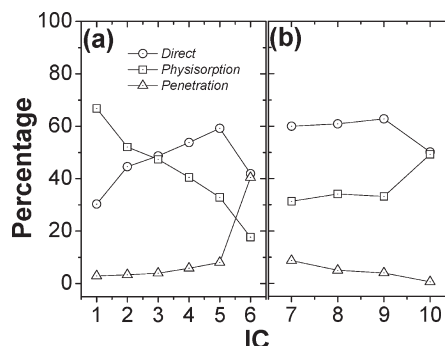


Figure 2. Percentages of the different collision events for the different initial conditions considered in this study.

both the minimum height of the projectile center-of-mass above the $\text{Au}\{111\}$ surface $h_{\text{NO},\min}$ and the number of inner turning points nITPs in the direction perpendicular to the surface that the projectile experiences during the collision with the surface. According to the first criterion, the trajectories can be classified as penetrating, when $h_{\text{NO},\min}$ drops below a certain height h_p , defined as $0.5(\langle h_{\text{CF}_3} \rangle + \langle h_{\text{CF}_2} \rangle)$, where h_{CF_3} and h_{CF_2} are the heights of the CF_3 and adjacent CF_2 groups in the monolayer, and they can be calculated in a molecular dynamics simulation at 300 K; the value of h_p thus obtained is 11.6 Å. The trajectories were additionally sorted according to nITPs into two different subsets, i.e., those with $n\text{ITPs} = 1$ and the remaining ones ($n\text{ITPs} > 1$). The former type is called here direct collision and the latter physisorption. In previous work on the scattering dynamics of $\text{CO}_2 + \text{F-SAM}$,⁵ it was found that in order to attain thermal accommodation of the CO_2 rotational degrees of freedom at least 15 ITPs were needed. This means that since the probability distribution plots of nITPs peak at $n\text{ITPs} = 2$ and show exponential decay with average values of 5–9,⁵ many of the $\text{CO}_2 + \text{F-SAM}$ physisorption trajectories behave pretty much in the same way as the direct ones and do not lead to thermal accommodation. This point is also discussed in this work below.

The percentages of the different trajectory types for the different ICs are plotted in Figure 2. As seen in Figure 2a, for ICs 1–5, the percentage of direct (physisorption) events increases (decreases) as a function of the collision energy, i.e., as it goes from IC 1 to IC 5, while the percentage of penetration remains almost constant. The percentages of trajectory types for ICs 7–10 are similar to those found for IC 5, except when the incident angle is 60° (IC 10), for which physisorption increases and the other two collision types decrease with respect to IC 5 and ICs 7–9. Surprisingly, for IC 6 ($E_i = 40$ kcal/mol) there is a sharp increase in the percentage of penetration (it goes from 8% for IC 5 to 40% for IC 6) at the expense of a decrease in both direct trajectories and physisorption. These collision energy dependencies of the collision types contrast with previous $\text{CO}_2 + \text{F-SAM}$ simulations, where the percentage of penetration was shown to decrease with E_i .⁵ However, for $\text{O}(\text{^3P}) + \text{F-SAM}$ Hase and co-workers also found that the percentage of penetration increases with the collision energy.⁶⁴ The explanation for the discrepancy between the NO and the $\text{CO}_2 + \text{F-SAM}$ systems relies on the fact that there are two different types of penetration: (a) events where the projectile penetrates the F-SAM in the first collision (direct penetration) and (b) when the projectile penetrates after being physisorbed on top of the surface for a while (physisorption penetration). In the present NO + F-SAM simulations more than 84% of the penetration events turn out to be direct,

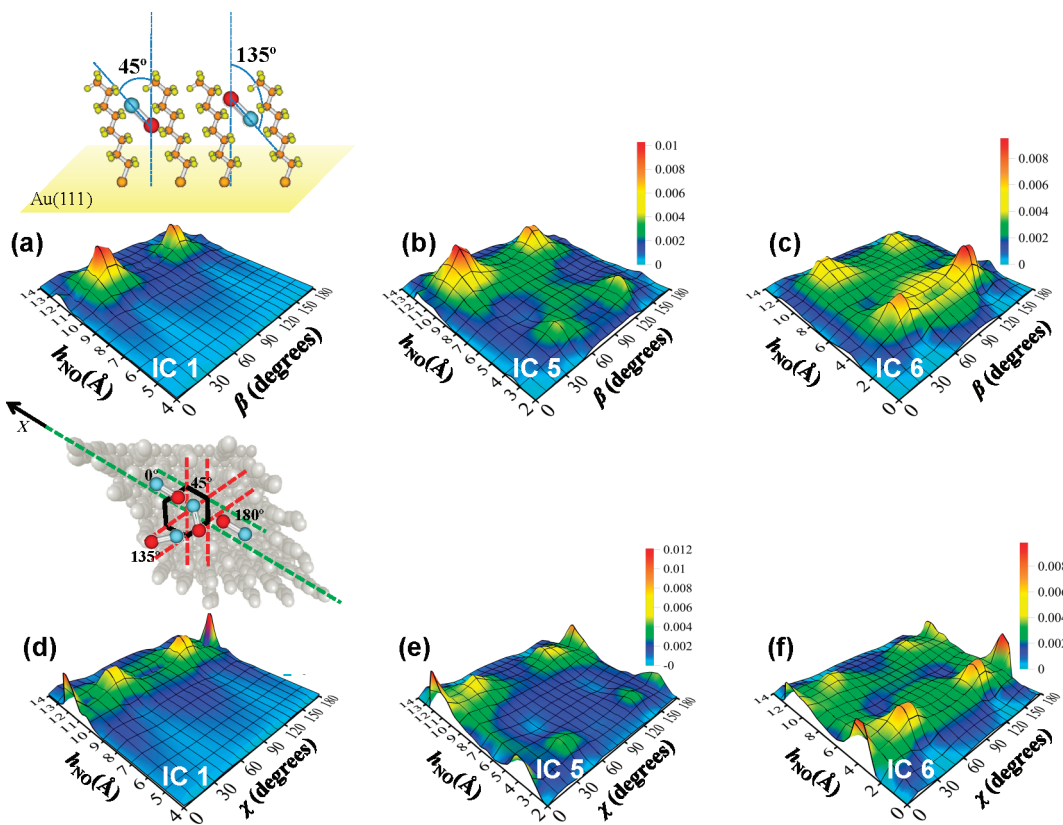


Figure 3. Probability density plots for the different configurations of the projectile inside the F-SAM. (a, b, and c) Probability vs the height of the projectile above the gold surface h_{NO} and the angle β formed between the O–N direction and the perpendicular to the surface for ICs 1, 5, and 6, respectively. (d, e, and f) Probability vs h_{NO} and the angle χ formed between the projection of the O–N direction onto the gold surface with the X axis (see the cartoon) for ICs 1, 5, and 6, respectively.

whereas in $\text{CO}_2 + \text{FSAM}$ direct penetration is much less important and ranges between 10% and 60%. When the percentage of direct penetration events was calculated as a function of E_i , this value increases for both projectiles NO and CO_2 scattering off F-SAM. Additionally, previous simulations in our research group on Ar scattering off an F-SAM go in the same direction, i.e., the percentage of direct penetration is 67% for $E_i = 12 \text{ kcal/mol}$ and 82% for $E_i = 24 \text{ kcal/mol}$. However, overall penetration is much less important in NO + F-SAM than in $\text{CO}_2 + \text{FSAM}$. For NO + F-SAM, penetration accounts for less than 10% of the collision types for ICs 1–5 ($E_i \leq 10.6 \text{ kcal/mol}$), while for $\text{CO}_2 + \text{F-SAM}$ this percentage ranges from 20% to 45%, in the same energy range. Additionally, penetration in $\text{CO}_2 + \text{F-SAM}$ is a much longer duration process than in NO + F-SAM. For $\text{CO}_2 + \text{F-SAM}$ the probability density function of the residence time $P(\tau)$ inside the monolayer peaks at $\tau = 20–25 \text{ ps}$ and extends up to 140 ps for $E_i = 10.6 \text{ kcal/mol}$,⁹ while for NO + F-SAM $P(\tau)$ shows a sharp peak at $\tau = 0–10 \text{ ps}$ and the tail extends up to 60 ps at the same collision energy (the plots are not shown here for simplicity). The strength of the gas–surface interaction affects the shape of the residence time distributions, i.e., CO_2 interacts more strongly than NO with the F-SAM. In general, big charged molecules are expected to interact strongly with the F-SAM and provide a very high sticking probability as well as long residence times. By way of example, Cooks and co-workers conducted experimental studies on $(\text{CH}_3)_2\text{SiNCS}^+$ scattering off an F-SAM and found that these cations remain trapped inside the monolayer for many hours.⁶⁸

Although the frequency of penetrating collisions is low in our simulations, it is of interest to analyze the behavior of the projectile

in the bulk of the monolayer. Figure 3 shows probability density plots as a function of the height of the projectile above the gold surface (h_{NO}), the angle formed between the O–N axis and the perpendicular to the surface (β), and the angle formed between the projection of the O–N axis onto the gold surface and the X axis (angle χ); the chains of the monolayer are tilted in the +X direction (see the cartoon of Figure 3d). Figure 3a–c shows probability functions depending on h_{NO} and β , whereas Figure 3d–f depend on h_{NO} and χ . The results indicate that the projectile penetrates just a few Angstroms inside the monolayer for the lowest collision energies, whereas for the highest E_i of 40 kcal/mol NO penetrates deeper and there seems to be a stable region at around 3–4 Å above the gold surface (Figure 3c and 3f). Figure 3 of the Supporting Information shows that for the NO molecules (with $E_i = 40 \text{ kcal/mol}$) to penetrate the monolayer they have to surmount a potential energy barrier, after which there is a minimum, thus explaining the accumulation of molecules in this area of the monolayer. Hase and co-workers also found that in a significant fraction of $\text{O}^{(\text{3P})} + \text{H-SAM}$ penetration events $\text{O}^{(\text{3P})}$ remained trapped close to the gold surface.⁶⁴ Our results and also Hase's results, however, may be affected by the approximate nature of the projectile–gold interactions described above. As the collision energy increases (from IC 1 to IC 6) the probability distributions become broader as the projectile has more energy to move around. In terms of the angle formed by the projectile with the normal there are two stable situations, drawn in a cartoon in Figure 3a. The maximum probabilities correspond to β angles that deviate from the 300 K equilibrium tilt angle of the F-SAM chains ($\sim 12^\circ$), i.e., the projectile

and the chains are not arranged in a parallel fashion (see Figure 3a). This is due to the important number of interactions taking place between the projectile and the surface atoms, which make β higher than the tilt of the F-SAM chains (45° vs 12°). Quite interestingly, for low incident energies the most stable situation corresponds to an angle β of 45° , i.e., with the O atom pointing downward, whereas for high incident energies the other orientation of $\beta = 135^\circ$ (O pointing upward) is the most stable one.

When the orientation of the projectile inside the monolayer is analyzed in terms of the angle χ , four maxima are obtained for a given value of h_{NO} . In this case the plots (Figure 3d–f) are symmetric for $\chi < 90^\circ$ and $\chi > 90^\circ$. The presence of the four peaks can be understood on the basis of the hexagonal package of the chains (see the cartoon of Figure 3a). In the absence of a tilt angle, the four maxima would be of the same intensity as the three different grooves formed between the chains (green and red dashed lines in the cartoon) would be equally accessible. The green grooves (parallel to the X axis) lead to χ angles of 0° or 180° , and the red grooves accommodate the molecules inside them with theoretical χ angles close to 60° and 120° (the actual values of the angles corresponding to these peaks are 15° off the theoretical value obtained from the hexagonal package). However, there is a tilt in the chains along the $+X$ direction, which makes the $\chi = 0^\circ$ or 180° orientation more easily for the projectile to achieve, as it can penetrate the monolayer along the perpendicular to the surface as it comes from the gas phase. However, in order to penetrate the red grooves, the molecule has to enter skew, which explains the lower intensity of the peaks at around 45° and 135° .

III.B. Rotational Quantum Number Distributions $P(J)$. Energy conservation dictates that the initial collision energy E_i equals the sum of the final translational energy of the projectile E_f and the changes in the internal ΔE_{int} and surface energies ΔE_{surf}

$$E_i = E_f + \Delta E_{\text{int}} + \Delta E_{\text{surf}} \quad (5)$$

For $\text{CO}_2 + \text{F-SAM}$, only rotational energy transfer contributed to ΔE_{int} with the vibrational states being adiabatic.^{4,5,9} In particular, CO_2 molecules initially excited to the (01^10) bend state, which is the lowest frequency mode of the molecule, preserve their initial excitation during the collision process in more than 90% of the collisions.⁴ In the present study, when NO is vibrationally excited to $v = 15$ at $E_i = 10.6$ kcal/mol, 99.6% of the molecules scatter off the F-SAM without loss of vibrational energy, with 0.4% losing only one quantum of vibration. This is an expected result on account of the previous behavior of the bend mode states of CO_2 and also due to the shorter interaction time in $\text{NO} + \text{F-SAM}$ compared with $\text{CO}_2 + \text{F-SAM}$ and to the high NO stretching frequency. Multiquantum vibrational transitions are possible when NO collides against a gold surface, due to nonadiabatic coupling of nuclear motion to electronic excitations of the metal surface.^{6,7,9}

Figure 4 shows probability plots for the rotational quantum numbers J of the scattered molecules $P(J)$. As in previous work, the $P(J)$ values were fit to a sum of two Boltzmann distributions of rotational states at the temperatures T_s and T

$$P(J) = a_{T_s} \frac{hcB}{kT_s} (2J + 1) \exp\left(-\frac{hcBJ(J + 1)}{kT_s}\right) + [1 - a_{T_s}] \frac{hcB}{kT} (2J + 1) \exp\left(-\frac{hcBJ(J + 1)}{kT}\right) \quad (6)$$

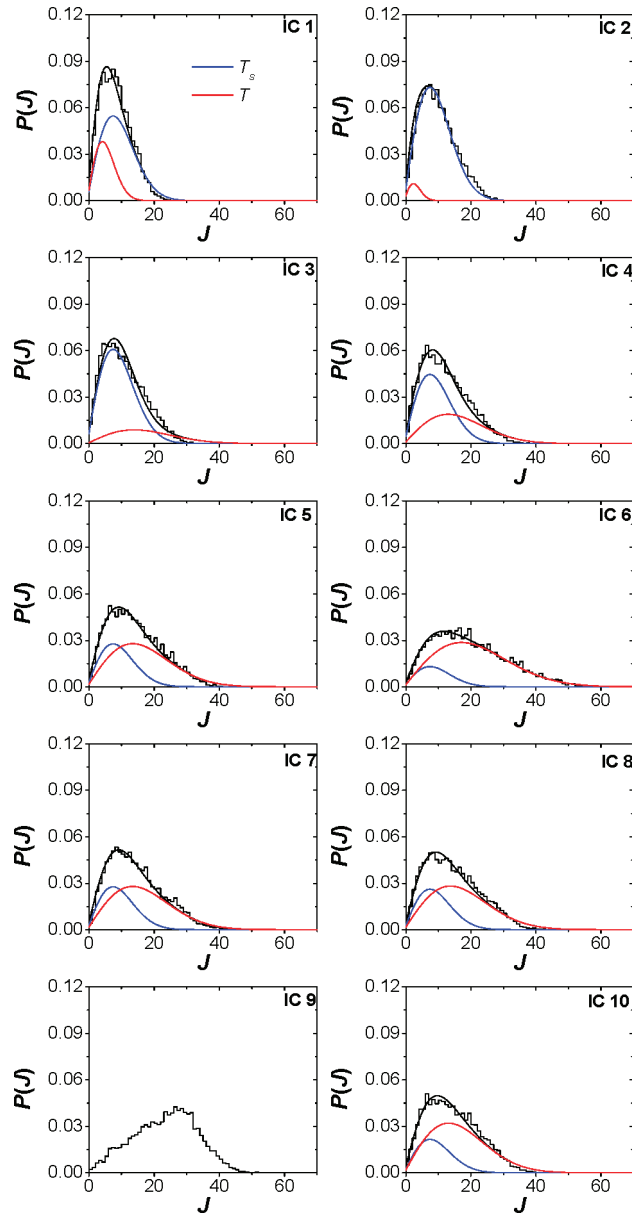


Figure 4. Probability density plots for the rotational quantum number J of the scattered NO molecules $P(J)$ for ICs 1–10. The histograms show the simulation results, the smooth black line is the fit to eq 6, and the red and blue lines are the first and second terms of the equation.

where $T_s = 300$ K and a_{T_s} and T are parameters in the fit. Table 3 collects the outcomes of the different fits. The histograms in Figure 4 are the simulation $P(J)$ results, the smooth black lines are the results of the fits, and the blue and red lines correspond to the first and second terms in eq 6, respectively. All simulation $P(J)$ results are well fit by eq 6 except those that resulting from IC 9 ($E_i = 10.6$ kcal/mol and $\theta_i = 60^\circ$).

The parameter a_{T_s} can be interpreted as the degree of thermal accommodation of the NO rotational degrees of freedom. Table 3 shows that a_{T_s} decreases with E_i (except for IC 1) and becomes 0 for IC 9. Our results do not show a perfect monotonic decrease of a_{T_s} with collision energy (there is an increase from IC 1 to IC 2) because, as indicated above, a_{T_s} is a parameter obtained from a nonlinear fit of the trajectory $P(J)$ data to eq 6. For $\text{CO}_2 + \text{F-SAM}$,⁵ the values of a_{T_s} obtained from either

Table 3. Parameters of the Boltzmann Fits to the $P(J)$ distributions

IC	$\alpha_{T_s}^a$	T
1	71 ± 8	104 ± 26
2	95 ± 2	38 ± 20
3	79 ± 11	993 ± 658
4	58 ± 9	875 ± 224
5	36 ± 6	935 ± 107
6	17 ± 2	1491 ± 74
7	36 ± 4	931 ± 73
8	34 ± 6	971 ± 112
9	0	
10	28 ± 7	896 ± 98

^a Expressed as percentage.

$P(J)$ or $P(E_f)$ also decrease monotonically (or almost monotonically) with collision energy, and this was attributed to the higher frequency of direct events (at high collision energies) that are not expected to be efficient attaining thermal accommodation. Our results indicate that thermalization of the rotational degrees of freedom is very efficient for IC 2. Actually, the average rotational energies of the scattered NO molecules for IC 2 is 0.61 kcal/mol, in close agreement with the theoretical value for a diatomic molecule that fully accommodates its rotational degrees of freedom ($RT_s = 0.6$ kcal/mol).

Some efforts have been unsuccessfully taken in the past to identify collision types with thermal accommodation mechanisms.^{5,8,17,20} Intuitively, larger duration collisions, i.e., physisorption and penetration, might lead to thermal accommodation, while short direct events can be thought of as processes that hardly achieve thermal accommodation. However, previous results show that α_{T_s} is not equivalent to either the fraction of physisorption or penetration events or their sum in Ar + F-SAM⁸ and CO₂ + F-SAM simulations.⁵ Additionally, the thermal accommodation coefficients extracted from the Boltzmann fits of the $P(J)$ or $P(E_f)$ distributions differ from each other in CO₂ + F-SAM.⁵ Furthermore, Hase and co-workers found that direct trajectories can also lead to thermal accommodation of the translational degrees of freedom in Ne scattering off a SAM surface.^{16,17,19}

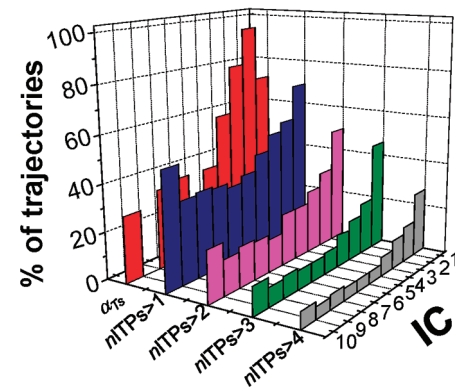
As seen in the previous section, the definition of the different collision mechanisms relies on counting the number of changes in the center-of-mass velocity vector of the projectile in the perpendicular axis (*nITPs*). Figure 5a shows the percentages of trajectories with *nITPs* > *i* (with *i* = 1–4) for the different ICs, in comparison with the values of α_{T_s} obtained from the fits to $P(J)$. The percentages of trajectories that fulfill the *nITPs* > *i* criterion do not match the α_{T_s} pattern for the different ICs. In particular, two important features of the α_{T_s} histogram are not captured with the *nITPs* analysis, i.e., the sharp decrease as a function of E_i (from IC 1 to IC 6) and the fact that α_{T_s} vanishes for IC 9.

Alternatively to the *nITPs* analysis, one may look at changes in the direction of the rotational angular momentum J of the NO molecule in the course of the dynamics. The change in the direction of J can be quantified by the angle Φ

$$\Phi = \cos^{-1} \left(\frac{\mathbf{J}(t) \cdot \mathbf{J}(t - \tau)}{|\mathbf{J}(t)| |\mathbf{J}(t - \tau)|} \right) \quad (7)$$

Where $\mathbf{J}(t)$ is the rotational angular momentum of the molecule at time t and τ is a time step of 30 fs. The number of times that each trajectory changes its rotational angular momentum by an

(a) *nITPs* analysis



(b) J analysis

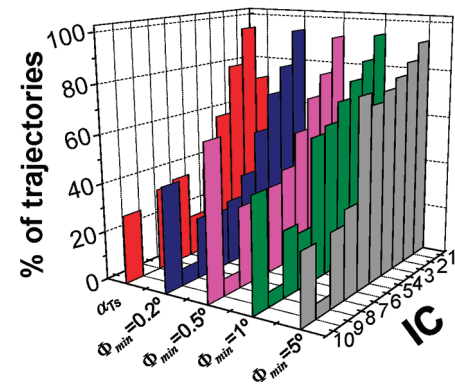


Figure 5. Percentages of trajectories that fulfill (a) *nITPs* analysis and (b) J analysis (see text) in comparison with the percentage of trajectories that thermalize rotation α_{T_s} , which was obtained from the $P(J)$ distributions.

angle greater than Φ_{\min} is denoted here as $n_{\Phi_{\min}}$. Additionally, the trajectories should perform a given number of these changes (denoted here as $n^*_{\Phi_{\min}}$) to attain thermal equilibrium. Thus, the percentage of trajectories for which $n_{\Phi_{\min}} > n^*_{\Phi_{\min}}$ is a measure of the thermal accommodation of the molecules and can be compared with α_{T_s} . Additionally, the values of $n^*_{\Phi_{\min}}$ can be optimized for each batch of trajectories by fitting the percentages of trajectories obtained as indicated above to the α_{T_s} values.

The values of $n^*_{\Phi_{\min}}$ were optimized separately for ICs 1–6 and ICs 7–10, as they refer to different initial rotational excitations of the molecule; the optimized values are collected in Table 4. Figure 5b shows the percentages of trajectories for which $n_{\Phi_{\min}} > n^*_{\Phi_{\min}}$ as a function of the values of Φ_{\min} .

As seen in Figure 5b, the above J analysis sorts the trajectories in a way that resembles the α_{T_s} pattern for the different ICs, particularly when Φ_{\min} is small.

The J analysis presented in this paper is superior than the *nITPs* analysis predicting the kind of collision events that lead to thermal accommodation. The J analysis shows that thermalization occurs after the projectile suffers a minimum number of gentle “kicks” that induce a very small change in J . This mechanism explains both the decrease in the thermal accommodation as a function of E_i (from IC 1 to IC 6) and the lack of thermal accommodation obtained for rotationally excited NO + F-SAM (IC 9). The former occurs because the gas–surface interaction time decreases as E_i increases. Thus, for low E_i an important number of changes in the direction of J may take place,

Table 4. Optimized Values of $n_{\Phi_{\min}}$ as a Function of Φ_{\min}^a

Φ_{\min}	$n_{\Phi_{\min}}^*$	
	ICs 1–6	ICs 7–10
0.2	31	40
0.5	20	28
1	12	23
5	5	10

^a For every trajectory the number of times that J changes, between two consecutive steps, by at least an angle Φ_{\min} was counted; this number is $n_{\Phi_{\min}}$. The percentages of trajectories shown in Figure 5 are those for which $n_{\Phi_{\min}} > n_{\Phi_{\min}}^*$, with $n_{\Phi_{\min}}^*$ being the values collected in this table that have been optimized to fit the α_{T_s} values of Table 3.

as the interaction time is long, even for direct events. Actually, for the lowest E_i up to 86% of the direct trajectories contribute to thermal accommodation according to the J analysis. This percentage diminishes to 18% for the highest collision energy (IC 6). The $\alpha_{T_s} = 0$ result for IC 9 can also be explained with the J analysis. When rotationally excited NO strikes the surface the direction of J changes abruptly, i.e., on average the values of Φ are higher than those found for the other ICs, and a minimum number of moderate changes in J is not achieved by many trajectories. According to our analysis, the time required for the molecule's rotational degrees of freedom to become thermally equilibrated is 0.93 ps for ICs 1–4 and 1.2 ps for the remaining ICs.

Finally, the rotational energies of the scattered molecules obtained in our study are compared with those obtained in the experiments.¹ The first comparison concerns the experimental $P(J)$ distributions (see Figure 6a and 6b). In the experimental study the rotational quantum number distributions are presented as logarithmic plots (see Figure 7a of ref 1 and Figure 6a of this paper) alongside with linear least-squares fits to the high-J part of the distributions ($J > 10$) to extract the rotational temperatures T_{rot} from the slopes.¹ The values of T_{rot} obtained in the experimental study are in good agreement with those obtained here using the same procedure (see Figure 6b). An additional analysis was done in the experimental work that deals with the probability δ of achieving 3.4 kcal/mol of rotational energy.¹ The experimental values of δ vary linearly with the incident velocity v_i . The slope of the experimental δ vs $1/v_i$ plot is -5.7×10^3 m/s (see Figure 9 of ref 1), which can be compared with the value $-(7.5 \pm 1.6) \times 10^3$ m/s obtained here. Last, a caviat: the experimental angular momentum J also includes internal (electronic and spin) angular momenta, which are neglected in our classical simulations. Additionally, the simulations are run on the A' potential energy surface, although both doublet levels should be considered in a more rigorous treatment. For these reasons, the comparisons made here with the experimental data can only be regarded as qualitative.

III.C. Translational Energy Distributions $P(E_f)$. If the NO translational degrees of freedom get fully accommodated as a consequence of the collisions with the F-SAM, a Boltzmann distribution of translational energies

$$P^{\text{Boltz}}(E_f) = \frac{1}{(kT_s)^2} E_f \exp\left(-\frac{E_f}{kT_s}\right) \quad (8)$$

would fit the translational energy distributions of the scattered molecules. However, eq 8 only fits the $P(E_f)$ distributions for ICs

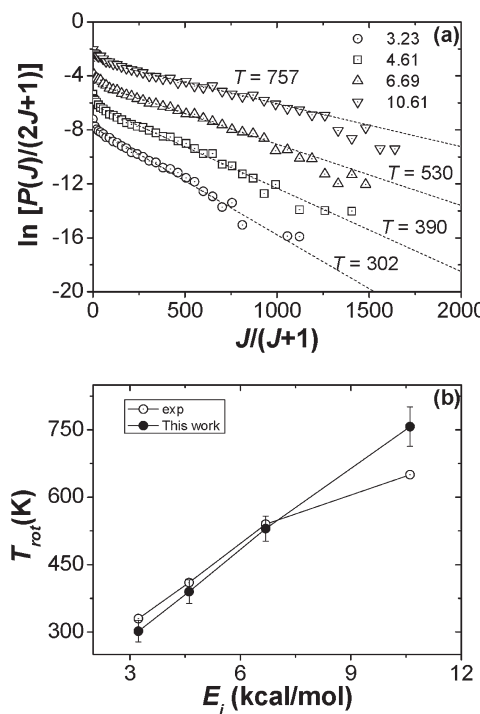


Figure 6. (a) Logarithmic linear plots (symbols) of the $P(J)$ distributions, and fit (dotted lines) to extract the rotational temperatures (b) in comparison with experimental results.

1–4 with temperatures different from T_s and being 268, 427, 542, and 779 K, respectively. The use of two Boltzmann components with different temperatures, either with one fixed at T_s and the other being a parameter or with both used as parameters, does not improve the fits. The temperature obtained for IC 1 (268 K) is closest to T_s and indicates that, under these conditions ($E_i = 1$ kcal/mol), the degree of thermal accommodation of the translational degrees of freedom is the highest (among the ICs of this study). For IC 1 the average translational energy of the scattered molecules $\langle E_f \rangle$ is 1.07 kcal/mol, slightly lower than the theoretical value of 1.2 kcal/mol ($2RT_s$) for full thermal accommodation. For ICs 2–4, the distributions are hyperthermal with values of $\langle E_f \rangle \gg 2RT_s$. This indicates that, in comparison with the rotational degrees of freedom, for translation motion it is harder to reach thermal equilibrium with the surface. Similar results have been obtained for CO₂ + FSAM, where the values of α_{T_s} obtained from $P(E_f)$ were systematically lower than those obtained from $P(J)$.⁵ For CO₂ + FSAM, both $P(E_f)$ and $P(J)$ are fit to a sum of two Boltzmann components, with the contribution of the Boltzmann component at T_s being always above 0.5 for $E_i \leq 10.6$ kcal/mol, whereas for NO + F-SAM only the $P(J)$ distributions are fit to two Boltzmann components. This result is a consequence of the stronger interaction of the CO₂ molecule vs NO with the F-SAM and the longer residence times, as indicated above.

III.D. Energy Transfer. Assuming that rotation and vibration are uncoupled, ΔE_{int} can be written as

$$\Delta E_{\text{int}} = \Delta E_{\text{rot}} + \Delta E_{\text{vib}} \quad (9)$$

where ΔE_{vib} and ΔE_{rot} are the changes in vibrational and rotational energies of NO, respectively. The average values of these quantities are shown in Figure 7a and 7b, respectively, as a

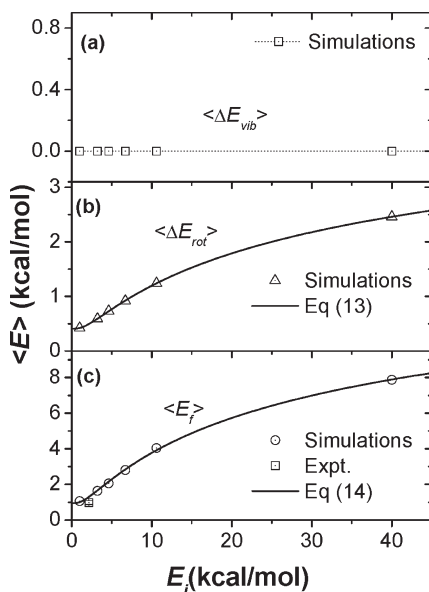


Figure 7. Average energy transfer to (a) vibrational, (b) rotational, and (c) translational energy of the projectile as a function of the collision energy in the NO + F-SAM scattering process (results correspond to ICs 1–6). Equations 13 and 14 are fit (solid lines) to the simulations results (symbols).

function of the incident energy E_i ; the results shown in Figure 7 correspond to the initial conditions ICs 1–6, i.e., $E_i = 1–40$ kcal/mol. As seen in the figure, NO vibration is adiabatic in the energy range of this study, while rotational energy transfer increases with E_i .

A simple model based on the adiabaticity parameter⁵¹ can be used to rationalize the energy transfer efficiencies found in our NO + F-SAM simulations. The adiabaticity parameter is defined as⁵¹

$$\xi = \frac{\tau_c}{t_{\text{rot(vib)}}} \quad (10)$$

where τ_c is the duration of the collision process and $t_{\text{rot(vib)}}$ is the rotational(vibrational) period of the diatomic molecule, depending on whether rotational or vibrational energy transfer is treated. The collision time τ_c can be expressed as a/v_i , where a is the “range” of the intermolecular force and v_i is the incident velocity of the projectile. The adiabaticity parameter is therefore inversely proportional to v_i

$$\xi = \frac{a}{v_i \tau_{\text{rot(vib)}}} \quad (11)$$

In the adiabatic limit ($\xi > 1$), the average (rotational or vibrational) energy transfer decreases exponentially with ξ^{51}

$$\langle \Delta E_{\text{rot, vib}} \rangle = \langle \Delta E_{\text{rot, vib}} \rangle^{\text{sudden}} \exp(-\xi) \quad (12)$$

where $\langle \Delta E_{\text{rot, vib}} \rangle^{\text{sudden}}$ is the average energy transfer in the sudden limit ($\xi = 0$). This model was proposed in the context of gas-phase atom + diatom collisions, and it needs to be adapted to gas–surface collisions. The above equation predicts no average energy transfer in the limit of low incident velocities, which is not the case in gas–surface collisions because of thermal desorption. Therefore, the simplest adjustment needed in eq 12 is the inclusion of an additional constant term that would account for energy transfer in the $v_i \rightarrow 0$ limit.

As indicated above $\langle \Delta E_{\text{vib}} \rangle$ is zero in the energy range of our study, and higher collision energies would be needed to obtain nonzero vibrational energy transfer. However, the $\langle \Delta E_{\text{rot}} \rangle$ values

increase significantly with the collision energy, and eq 12 (adapted as indicated in the previous paragraph) can be used to model rotational energy transfer in NO + F-SAM

$$\langle \Delta E_{\text{rot}} \rangle = \langle \Delta E_{\text{rot}} \rangle^{\text{sudden}} \times \exp\left(-\frac{b_{\text{rot}}}{\sqrt{E_i}}\right) + c_{\text{rot}} RT_s \quad (13)$$

where $\langle \Delta E_{\text{rot}} \rangle^{\text{sudden}}$ is the high- E_i limiting value for $\langle \Delta E_{\text{rot}} \rangle$ and b_{rot} is another parameter than contains a, t_{rot} [from eq 11], and the mass of the projectile m . Since ξ is proportional to b_{rot} , high values of b_{rot} are associated with adiabatic energy transfer. An additional parameter c_{rot} multiplying RT_s accounts for the degree of thermal accommodation in the $v_i \rightarrow 0$ limit.

As seen in Figure 7b, eq 13 reproduces very well the simulation results. The resulting fitting parameters are $\langle \Delta E_{\text{rot}} \rangle^{\text{sudden}} = 5.35 \pm 0.02$ kcal/mol, $b_{\text{rot}} = 6.06 \pm 0.02$ (kcal/mol)^{1/2}, and $c_{\text{rot}} = 0.68 \pm 0.00$.

The average E_f values obtained in our work show a similar E_i dependence as $\langle \Delta E_{\text{rot}} \rangle$. For this reason, the same exponential function (eq 12) was employed to fit $\langle E_f \rangle$, slightly adapted to account for the theoretical value $2RT_s$ (rather than RT_s) obtained for full accommodation of the translational degrees of freedom

$$\langle E_f \rangle = \langle E_f \rangle^{\text{sudden}} \times \exp\left(-\frac{b_f}{\sqrt{E_i}}\right) + c_f (2RT_s) \quad (14)$$

The parameters of eq 14 have the same physical meaning as those of eq 13. As seen in Figure 7c, eq 14 is also able to reproduce the computed $\langle E_f \rangle$ values. The parameters obtained in the fit are $\langle E_f \rangle^{\text{sudden}} = 17.08 \pm 0.61$ kcal/mol, $b_f = 5.69 \pm 0.24$ (kcal/mol)^{1/2}, and $c_f = 0.79 \pm 0.10$.

For completeness and to show the accuracy of our simulations, Figure 7c also shows an experimental result² (open square) that falls pretty close to the model results.

According to this model, both $\langle \Delta E_{\text{rot}} \rangle$ and $\langle E_f \rangle$ plateau at the limiting values of 5.5 and 18.0 kcal/mol, respectively. However, the absence of more data for high E_i precludes a definite conclusion about energy transfer efficiencies in the high- E_i regime. On the other hand, as state above, the exponential behavior of eq 12 is known to be valid in the adiabatic regime (low E_i values). For high E_i , the sudden limit is reached and the applicability of eq 12 is uncertain.

Energy transfer to the F-SAM surface has been studied in the past by Hase and co-workers⁷ and Morris and co-workers³⁴ using Ar, CO₂, and peptides as projectiles. They obtained very high efficiencies of energy transfer to the surface in the high collision energy limit. When this efficiency is expressed as $\langle \Delta E_{\text{surf}} \rangle/E_i$ the limiting values they obtained in their systems range from 0.7 to 0.98. The model employed here for $\langle \Delta E_{\text{rot}} \rangle$ and $\langle E_f \rangle$ provides the following expression for $\langle \Delta E_{\text{surf}} \rangle/E_i$

$$\frac{\langle \Delta E_{\text{surf}} \rangle}{E_i} = 1 - \frac{\langle \Delta E \rangle^{\text{sudden}} \times \exp\left(-\frac{b}{\sqrt{E_i}}\right) + c}{E_i} \quad (15)$$

Equations 5, 9, 13, and 14 were used to arrive at eq 15. The parameters in the equation are related to those of eqs 13 and 14; $c = c_{\text{rot}} RT_s + c_f (2RT_s)$, $\langle \Delta E \rangle^{\text{sudden}} = \langle \Delta E_{\text{rot}} \rangle^{\text{sudden}} + \langle E_f \rangle^{\text{sudden}}$, and $b \cong b_{\text{rot}} \cong b_f$. Equation 15 was fit to the simulation $\langle \Delta E_{\text{surf}} \rangle/E_i$ data obtaining the following fitting parameters: $c = 1.42 \pm 0.01$ kcal/mol, $\langle \Delta E \rangle^{\text{sudden}} = 24.5 \pm 1.5$ kcal/mol, and $b = 6.13 \pm 0.16$ (kcal/mol)^{1/2}. The fit is shown in Figure 8.

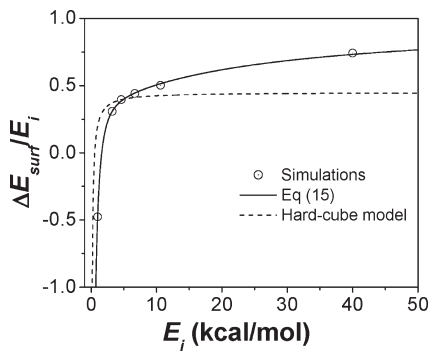


Figure 8. Average energy transfer to the surface relative to the collision energy E_i as a function of E_i in the NO + F-SAM scattering process. Equation 15 and the hard-cube model are fit (solid and dashed lines, respectively) to the simulation results (circles).

It is instructive to compare the results of the model presented here with those obtained with other models. One of the most commonly used models to study energy transfer in gas–surface collisions is the hard-cube model.⁷¹ According to the hard-cube model the energy transfer efficiency to the surface reads⁷¹

$$\left(\frac{\langle\Delta E_{\text{surf}}\rangle}{E_i}\right)^{\text{hard-cube}} = \frac{4\mu}{(\mu+1)^2} - \frac{\mu(2-\mu)}{(\mu+1)^2} \frac{2RT_s}{E_i} \quad (16)$$

where μ is m/M , with M being an effective surface mass. As seen in the figure, the hard-cube model is not able to reproduce the simulation data and the resulting value of μ is 0.15.

The model employed in the present paper predicts 100% efficiency of energy transfer to the surface at the high- E_i limit, i.e., $\langle\Delta E_{\text{surf}}\rangle/E_i = 1$ for $E_i \rightarrow \infty$. An additional fit was done with a constant term d included in the right-hand side of eq 15 to investigate possible deviations from the 100% efficiency in the $E_i \rightarrow \infty$ limit. The resulting fit provides a value of 0.00 for d , which corroborates the result. Previous studies showed limiting energy transfer efficiencies to the surface of 80–90% for peptides and CO₂ colliding with F-SAM surfaces.^{5,7} However, these values were obtained using $\langle\Delta E_{\text{surf}}\rangle/E_i = a \times \exp(-b/E_i)$ to fit the simulation results. In fact, if eq 15, with an additional constant parameter to account for possible deviations from the 100% efficiency in the high- E_i limit, is used instead to refit the CO₂ + F-SAM simulation results, a value of 1.02 ± 0.06 is obtained in the $E_i \rightarrow \infty$ limit. This result agrees with the value 1.00 found here for NO + F-SAM.

Experimental studies on rare gases scattering off gold and platinum surfaces⁷² in the energy range 1–4000 eV point also to limiting efficiencies of 100% or close to 100% for energy transfer to the surface. Moreover, recent simulation results in our research group on Ar + F-SAM⁷³ show that eq 15 is able to fit the energy transfer efficiencies up to very high energies (1500 kcal/mol) with a value for $\langle\Delta E_{\text{surf}}\rangle/E_i$ in the high- E_i limit of 1.00 ± 0.01 .

However, the highest E_i value in our NO + F-SAM simulation study was only 40 kcal/mol. Also, there is an uncertainty in the applicability of the model for high collision energies, which does not guarantee the correctness of eq 15 at very high E_i in NO + F-SAM. An additional factor that makes extrapolation to high collision energies uncertain is the fact that vibrational energy

Table 5. Lowest Order Orientation and Alignment Moments of the J Distribution

moments	classical mechanical value
A_0	$\langle 3J_z^2/ J ^2 \rangle - 1$
A_{1+}	$\langle 2J_z J_z/ J ^2 \rangle$
A_{2+}	$\langle (J_x^2 - J_y^2)/ J ^2 \rangle$
O_{1-}	$\langle J_y J \rangle$

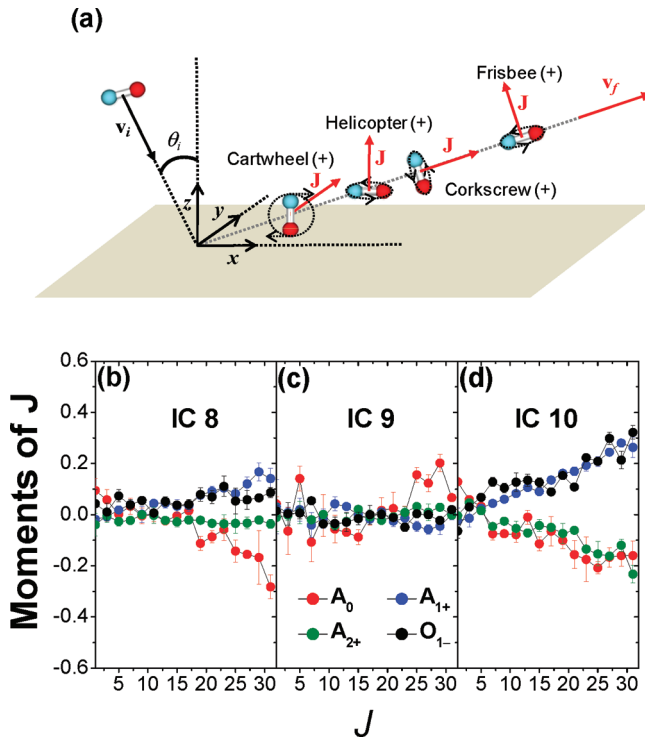


Figure 9. (a) Cartesian coordinate frame employed in the stereodynamics analysis and different rotational motions of the scattered projectile identified in the NO + F-SAM study. The lowest order orientation and alignment moments of the J distribution are plotted as a function of J for (b) IC 8, (c) IC 9, and (d) IC 10. Figure 9a is based in Figure 2 of ref 33.

transfer is expected to occur at the highest energies, a process that will compete with energy transfer to the surface.

III.E. Stereodynamics. Alignment and orientation of the scattered NO molecules are studied in this section. In particular, the lowest tensor A_0 , A_{1+} , and A_{2+} alignment moments and the O_{1-} orientation moment of the J distribution are computed for ICs 8–10 as in previous work on CO₂ scattering off a liquid surface and F-SAM.⁴³ This allows us to make a direct comparison between the stereodynamics of the NO + F-SAM and CO₂ + F-SAM systems. The classical mechanical analogues of the A_0 , A_{1+} , A_{2+} , and O_{1-} moments are collected in Table 5; the Cartesian coordinate frame as well as the different limiting types of rotational motion are depicted graphically in the cartoon of Figure 9a. The z axis is perpendicular to the surface, and the incident molecules move in the positive x direction (xz plane). In our simulations the xz plane is not fixed as the azimuthal angle is randomly sampled between 0° and 360° for each trajectory.

The values of the A_0 moment indicate whether J is preferentially perpendicular to the surface $A_0 > 0$, i.e., helicopter rotational motion,

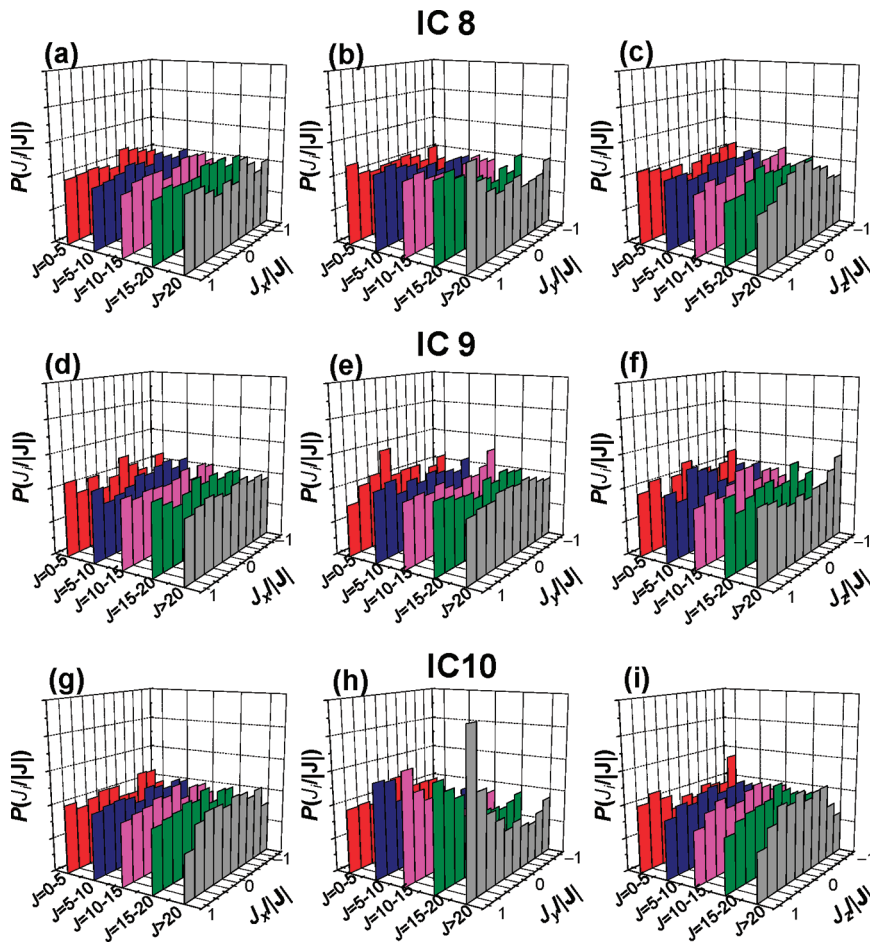


Figure 10. Probability density plots of the projection of the rotational angular momentum of the projectile \mathbf{J} onto the three Cartesian axes defined in Figure 9a as a function of the final values of J for IC 8 (a–c), IC 9 (d–f), and IC 10 (g–i).

or if \mathbf{J} is preferentially parallel to the surface $A_0 < 0$, i.e., cartwheel rotational motion. Analysis of the A_{2+} moments gives the relative contribution of in-plane (xz) and out-of-plane cartwheel behavior. The former occurs when A_{2+} is negative.

The O_{1-} moment is nonzero when the molecule scatters off the surface in a cartwheel fashion, and there is a preferred orientation of \mathbf{J} with respect to the y axis. In particular, O_{1-} is positive when the cartwheel rotation motion is such that NO spins with forward tumbling (cartwheel topspin motion).

Perkins and Nesbitt⁴³ and Troya and co-workers³³ have shown that the values of the orientation and alignment moments depend very strongly on the final angular momentum quantum number J for $\text{CO}_2 + \text{F-SAM}$ and $\text{CO} + \text{F-SAM}$, respectively. Thus, in Figure 9b–d, the lowest alignment and orientation moments are depicted as a function of J for ICs 8–10. In most cases, these moments increase (or decrease) their values as J increases, i.e., alignment and orientation increase as J increases. This result can be understood in terms of the \mathbf{J} analysis employed above to interpret the degree of thermal accommodation obtained from the $P(J)$ distributions. NO molecules have to suffer a minimum number of gentle “kicks” that change slightly the direction of \mathbf{J} in order to randomize the direction of \mathbf{J} . As discussed in previous sections, these events contribute mostly to the low- J part of the $P(J)$ distribution. Therefore, those NO molecules that scatter off the surface with low values of J will tend to randomize \mathbf{J} and the degree of alignment and orientation of \mathbf{J}

will be small. On the other hand, the molecules that scatter from the F-SAM rotationally excited will not randomize \mathbf{J} completely and will give rise to alignment and orientation of \mathbf{J} .

The results of Figure 9a and 9c for IC 8 and 10, respectively, indicate that NO tends to scatter off the surface in a cartwheel topspin fashion when it is rotationally excited because $A_0 < 0$ and O_{1-} is positive. This tendency is enhanced when the incident angle increases (for IC 10 when $\theta_i = 60^\circ$). The orientation of the angular momentum vector is analyzed in more detail in Figure 10, where probability distribution plots of the projections of \mathbf{J} onto the x , y , and z axes are shown for ICs 8–10. While the plots for the J_x and J_z projections are rather symmetric, the $P(J_y/J)$ plots for ICs 8 and 10 peak close to 1 as J increases, particularly for IC 10, indicating the preference for cartwheel topspin behavior of the scattered molecules. These results agree with the $\text{CO} + \text{F-SAM}$ simulation study of Troya and co-workers³³ for similar initial conditions. The values of the A_0 moments for $\text{CO} + \text{F-SAM}$ are -0.2 and -0.3 for θ_i of 30° and 60° , respectively, for $J > 20$, which compare well with the values of the present study that range from -0.1 to -0.3 . The $\text{CO} + \text{F-SAM}$ results of Troya and co-workers and our NO + F-SAM results contrast, however, with those for $\text{CO}_2 + \text{F-SAM}$, where a preference for helicopter behavior was found for $J > 60$ with cartwheel behavior arising for the higher J values.⁴³

The negative values of the alignment A_{2+} moment indicate that cartwheel rotational motion takes place, primarily, in the xz

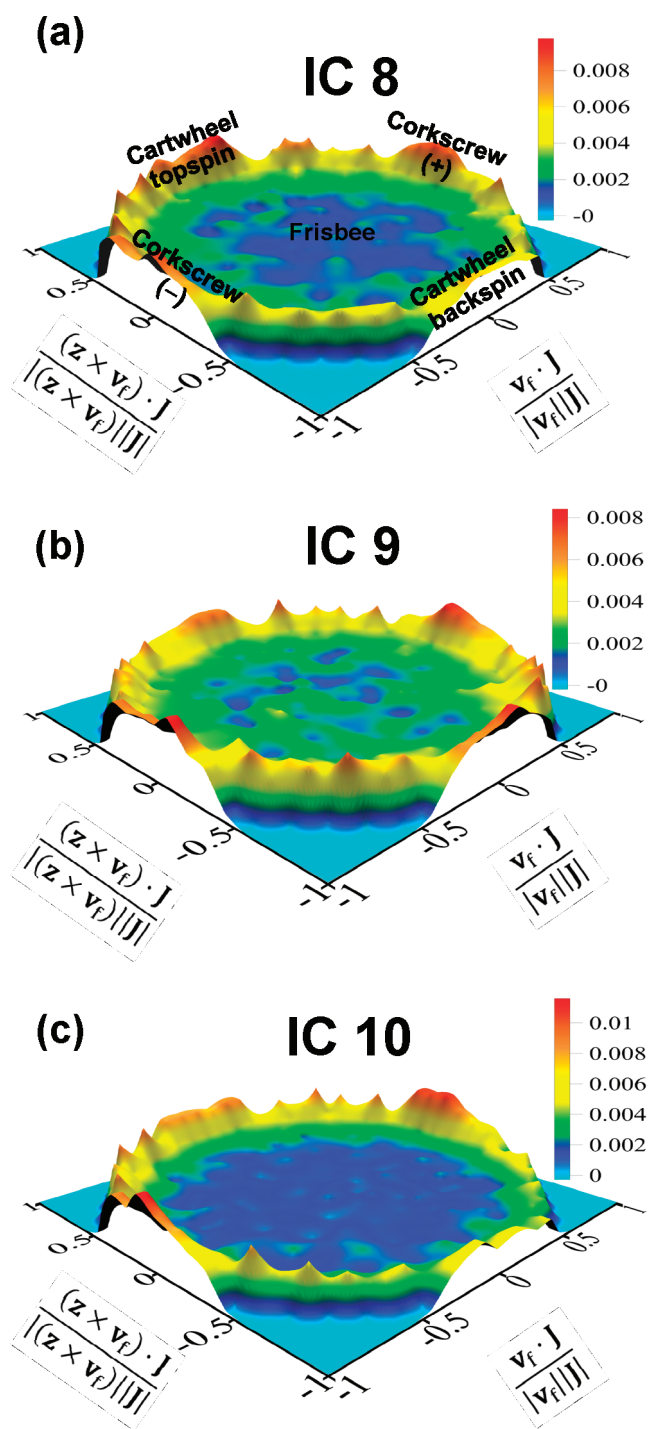


Figure 11. Probability density plots of the different rotational motions of the scattered NO molecules to distinguish among frisbee, cartwheel, and corkscrew motions. The probability is calculated as a function of the cosines of the angles formed between v_f and J and between $(z \times v_f)$ and J : a, b, and c refer to ICs 8, 9, and 10, respectively.

plane for $\theta_i = 60^\circ$ (IC 10), whereas for $\theta_i = 30^\circ$ (IC 8) the xz and yz planes are equally probable for cartwheel behavior, as the values of A_{2+} are close to 0.

When rotationally excited NO molecules strike the F-SAM (IC 9) the behavior of the scattered species is different. In particular, all moments studied here are close to 0 for all J values,

except A_0 that is slightly positive for $J > 25$, indicating helicopter behavior. This is an important difference with respect to the scattering of rotationally cold molecules colliding with F-SAM (ICs 8 and 10). Again, our result parallels those previously found by Troya and co-workers in their CO + F-SAM study.³³ The preference for helicopter rather than cartwheel behavior of the rotationally excited molecules was analyzed in detail in Troya's work.³³ Basically, rotationally excited molecules that strike the surface in a helicopter fashion tend to preserve their rotational excitation and conserve the alignment. On the other hand, those impinging the surface in a cartwheel fashion will deactivate more easily the initial rotational excitation, which will decrease cartwheel alignment.

Finally, the other two types of rotational motion of the scattered molecules shown in Figure 9a, frisbee and corkscrew, can only be examined by a further analysis of the projection of J onto the velocity of the scattering molecules v_f . Corkscrew (+) and (-) behavior occurs when J and v_f are parallel and antiparallel to each other, respectively, and frisbee rotational motion takes place when both vectors are perpendicular to each other, with frisbee (+) defined as in Figure 9a. Frisbee and cartwheel behaviors can be distinguished from each other by adding a third vector that goes along the z axis and will be called z here. Thus, frisbee motion is defined when the angle formed between J and a vector perpendicular to z and v_f (defined here as $z \times v_f$) is 90° ; when this angle is 0° (or 180°) the motion is pure cartwheel (+) [or (-)]. Figure 11 shows probability distribution plots for ICs 8–10 of the cosines of the following two angles: (1) the angle formed between v_f and J and (2) the one formed between $(z \times v_f)$ and J .

The results of Figure 11 indicate that cartwheel and corkscrew types of motion are slightly more probable than frisbee for all ICs. Cartwheel topspin is also more probable than cartwheel backspin for ICs 8 and 10, and both have the same probability for IC 9, which agrees with values of the O_{1-} moments seen before. Corkscrew motion has the same probability as cartwheel motion or slightly higher, particularly for ICs 9 and 10, with both orientations (+) and (-) being equally probable. The most (least) isotropic plot is that for IC 9 (IC 10), indicating less (more) orientation and alignment, in agreement again with the above analysis of the moments of the J distribution. Troya and co-workers also found preference for both cartwheel and corkscrew behavior vs frisbee motion in their CO + F-SAM simulations.³³

IV. CONCLUSIONS

Chemical dynamics simulations were performed to study the collision dynamics of the NO + F-SAM system. A potential energy function for the interaction between the projectile and the surface was developed from a fit to high-level ab initio calculations. The simulations indicate that the scattered projectiles display non-Boltzmann $P(E_f)$ distributions for all ICs except 1–4, and $P(J)$ distributions modeled by a sum of two Boltzmann components, one of them with a temperature T_s , which indicates a higher degree of thermal accommodation of rotation vs translation. The same result was found previously for $\text{CO}_2 + \text{F-SAM}$. Thermal accommodation of the rotational degrees of freedom in NO + F-SAM can be understood in terms of a minimum number of moderate variations in the direction of the rotational angular momentum of the molecule J in the course of the dynamics. This type of analysis provides a much better metric than previously used analyses based on the variation of the center-of-mass velocity vector of the projectile in the perpendicular direction.

A new model that accounts for energy transfer to the various degrees of freedom of the molecule and the surface is presented in this paper. The model is based on the adiabaticity parameter and on an $\exp(-a/v_i)$ dependence of energy transfer with the collision velocity v_i . It reproduces very well the simulation data in the collision energy range employed in this study (from 1 to 40 kcal/mol) and predicts 100% efficiency of energy transfer to the surface in the high collision energy limit. However, the absence of more simulation results for higher energies and the fact that the use of the exponential function is unclear for high energies indicate that the result of the extrapolation should be taken with caution.

The stereodynamics of the title process was also investigated here. In agreement with previous results for the CO + F-SAM system, the two preferred rotational motions of the scattered molecules are corkscrew and cartwheel. For corkscrew motion, both orientations of J are equally probable, whereas for cartwheel motion, the topspin orientation clearly dominates, particularly for high rotational states. Orientation and alignment are enhanced for higher incident angles.

Finally, the available experimental data was compared with the present simulation results, and good agreement was found in all cases, which supports the methods employed in the present paper.

ASSOCIATED CONTENT

Supporting Information. UCCSD(T)/aug-cc-pVDZ ab initio calculations of the A' and A'' potential energy surfaces of the NO + CF₄ system; experimental $P(J)$ distribution and fit; average potential energy calculated as a function of the height of the NO center of mass for the penetrating trajectories of IC 6. This material is available free of charge via the Internet at <http://pubs.acs.org>.

AUTHOR INFORMATION

Corresponding Author

*E-mail: emilio.nunez@usc.es.

ACKNOWLEDGMENT

The authors thank “Ministerio de Educación y Ciencia” (Grant No. CTQ2009-12588) and “Xunta de Galicia” (Grant No. PGDIT07PXIB209072PR). J.J.N. acknowledges the University of Santiago de Compostela for financial support through a Ph.D. fellowship. The authors also thank the “Centro de Supercomputación de Galicia (CESGA)” for use of their facilities.

REFERENCES

- (1) Cohen, S. R.; Naaman, R.; Sagiv, J. *J. Chem. Phys.* **1988**, *88*, 2757.
- (2) Cohen, S. R.; Naaman, R.; Sagiv, J. *Phys. Rev. Lett.* **1987**, *58*, 1208.
- (3) Nogueira, J. J.; Sanchez-Coronilla, A.; Marques, J. M. C.; Hase, W. L.; Martinez-Nunez, E.; Vazquez, S. A. *Chem. Phys.* **2011** in press.
- (4) Nogueira, J. J.; Vazquez, S. A.; Lourderaj, U.; Hase, W. L.; Martinez-Nunez, E. *J. Phys. Chem. C* **2010**, *114*, 18455.
- (5) Nogueira, J. J.; Vazquez, S. A.; Mazyar, O. A.; Hase, W. L.; Perkins, B. G.; Nesbitt, D. J.; Martinez-Nunez, E. *J. Phys. Chem. A* **2009**, *113*, 3850.
- (6) Nogueira, J. J.; Martinez-Nunez, E.; Vazquez, S. A. *J. Phys. Chem. C* **2009**, *113*, 3300.
- (7) Yang, L.; Mazyar, O. A.; Lourderaj, U.; Wang, J. P.; Rodgers, M. T.; Martinez-Nunez, E.; Addepalli, S. V.; Hase, W. L. *J. Phys. Chem. C* **2008**, *112*, 9377.
- (8) Vazquez, S. A.; Morris, J. R.; Rahaman, A.; Mazyar, O. A.; Vayner, G.; Addepalli, S. V.; Hase, W. L.; Martinez-Nunez, E. *J. Phys. Chem. A* **2007**, *111*, 12785.
- (9) Martinez-Nunez, E.; Rahaman, A.; Hase, W. L. *J. Phys. Chem. C* **2007**, *111*, 354.
- (10) Paz, Y.; Naaman, R. *J. Chem. Phys.* **1991**, *94*, 4921.
- (11) Day, B. S.; Shuler, S. F.; Ducre, A.; Morris, J. R. *J. Chem. Phys.* **2003**, *119*, 8084.
- (12) Gibson, K. D.; Isa, N.; Sibener, S. J. *J. Chem. Phys.* **2003**, *119*, 13083.
- (13) Day, B. S.; Morris, J. R. *J. Phys. Chem. B* **2003**, *107*, 7120.
- (14) Isa, N.; Gibson, K. D.; Yan, T.; Hase, W.; Sibener, S. J. *J. Chem. Phys.* **2004**, *120*, 2417.
- (15) Day, B. S.; Morris, J. R. *J. Chem. Phys.* **2005**, *122*, 234714.
- (16) Yan, T.; Hase, W. L. *Phys. Chem. Chem. Phys.* **2000**, *2*, 901.
- (17) Yan, T.; Hase, W. L.; Barker, J. R. *Chem. Phys. Lett.* **2000**, *329*, 84.
- (18) Yan, T.; Hase, W. L. *J. Phys. Chem. A* **2001**, *105*, 2617.
- (19) Yan, T.; Hase, W. L. *J. Phys. Chem. B* **2002**, *106*, 8029.
- (20) Yan, T.; Isa, N.; Gibson, K. D.; Sibener, S. J.; Hase, W. L. *J. Phys. Chem. A* **2003**, *107*, 10600.
- (21) Day, B. S.; Morris, J. R.; Troya, D. *J. Chem. Phys.* **2005**, *122*, 214712.
- (22) Day, B. S.; Morris, J. R.; Alexander, W. A.; Troya, D. *J. Phys. Chem. A* **2006**, *110*, 1319.
- (23) Shuler, S. F.; Davis, G. M.; Morris, J. R. *J. Chem. Phys.* **2002**, *116*, 9147.
- (24) Ferguson, M. K.; Lohr, J. R.; Day, B. S.; Morris, J. R. *Phys. Rev. Lett.* **2004**, *92*, 732011.
- (25) Li, G.; Bosio, S. B. M.; Hase, W. L. *J. Mol. Struct.* **2000**, *556*, 43.
- (26) Troya, D.; Schatz, G. C. *J. Chem. Phys.* **2004**, *120*, 7696.
- (27) Tasic, U.; Yan, T.; Hase, W. L. *J. Phys. Chem. B* **2006**, *110*, 11863.
- (28) Wainhaus, S. B.; Lim, H.; Schultz, D. G.; Hanley, L. *J. Chem. Phys.* **1997**, *106*, 10329.
- (29) Schultz, D. G.; Wainhaus, S. B.; Hanley, L.; DeSainteClaire, P.; Hase, W. L. *J. Chem. Phys.* **1997**, *106*, 10337.
- (30) Laskin, J.; Futrell, J. H. *J. Chem. Phys.* **2003**, *119*, 3413.
- (31) Meroueh, O.; Hase, W. L. *J. Am. Chem. Soc.* **2002**, *124*, 1524.
- (32) Troya, D.; Schatz, G. C. *Int. Rev. Phys. Chem.* **2004**, *23*, 341.
- (33) Alexander, W. A.; Morris, J. R.; Troya, D. *J. Phys. Chem. A* **2009**, *113*, 4155.
- (34) Lu, J. W.; Alexander, W. A.; Morris, J. R. *Phys. Chem. Chem. Phys.* **2010**, *12*, 12533.
- (35) Perkins, B. G.; Haber, T.; Nesbitt, D. J. *J. Phys. Chem. B* **2005**, *109*, 16396.
- (36) Perkins, B. G.; Nesbitt, D. J. *J. Phys. Chem. B* **2006**, *110*, 17126.
- (37) Zolot, A. M.; Harper, W. W.; Perkins, B. G.; Dagdigian, P. J.; Nesbitt, D. J. *J. Chem. Phys.* **2006**, *125*.
- (38) Perkins, B. G.; Nesbitt, D. J. *J. Phys. Chem. A* **2007**, *111*, 7420.
- (39) Perkins, B. G.; Nesbitt, D. J. *Proc. Natl. Acad. Sci. U.S.A.* **2008**, *105*, 12684.
- (40) Perkins, B. G.; Nesbitt, D. J. *J. Phys. Chem. A* **2008**, *112*, 9324.
- (41) Perkins, B. G.; Nesbitt, D. J. *J. Phys. Chem. B* **2008**, *112*, 507.
- (42) Perkins, B. G.; Nesbitt, D. J. *J. Phys. Chem. A* **2009**, *113*, 4613.
- (43) Perkins, B. G.; Nesbitt, D. J. *J. Phys. Chem. A* **2010**, *114*, 1398.
- (44) Los, J.; Gleeson, M. A.; Koppers, W. R.; Weeding, T. L.; Kleyn, A. W. *J. Chem. Phys.* **1999**, *111*, 11080.
- (45) Koppers, W. R.; Beijersbergen, J. H. M.; Weeding, T. L.; Kistemaker, P. G.; Kleyn, A. W. *J. Chem. Phys.* **1997**, *107*, 10736.
- (46) Koppers, W. R.; Gleeson, M. A.; Lourenço, J.; Weeding, T. L.; Los, J.; Kleyn, A. W. *J. Chem. Phys.* **1999**, *110*, 2588.
- (47) TD is often referred to as trapping desorption, but chemical dynamics simulations have shown it is better to call it thermal desorption.
- (48) Tasic, U.; Day, B. S.; Yan, T.; Morris, J. R.; Hase, W. L. *J. Phys. Chem. C* **2008**, *112*, 476.
- (49) Wang, J.; Meroueh, S. O.; Wang, Y.; Hase, W. L. *Int. J. Mass Spectrom.* **2003**, *230*, 57.

- (50) Song, K.; Meroueh, O.; Hase, W. L. *J. Chem. Phys.* **2003**, *118*, 2893.
- (51) Levine, R. D. *Molecular Reaction Dynamics*; Cambridge University Press: Cambridge, 2005.
- (52) Huber, K. P.; Herzberg, G. *Constants of Diatomic Molecules*; Van Nostrand: New York, 1979.
- (53) Vayner, G.; Alexeev, Y.; Wang, J.; Windus, T. L.; Hase, W. L. *J. Phys. Chem. A* **2006**, *110*, 3174.
- (54) Wang, J.; Hase, W. L. *J. Phys. Chem. B* **2005**, *109*, 8320.
- (55) Alexander, W. A.; Troya, D. *J. Phys. Chem. A* **2006**, *110*, 10834.
- (56) Alexander, M. A. *J. Chem. Phys.* **1991**, *94*, 8468.
- (57) Knowles, P. J.; Hampel, C.; Werner, H.-J. *J. Chem. Phys.* **1993**, *99*, 5219.
- (58) Werner, H.-J.; Knowles, P. J.; Lindh, R.; Manby, F.; Shutz, M.; et al. *MOLPRO, version 2008.1, a package of ab initio programs*; 2008.
- (59) Aoiz, F. J.; Verdasco, J. E.; Herrero, V. J.; Sáez Rábanos, V.; Alexander, M. A. *J. Chem. Phys.* **2003**, *119*, 5860.
- (60) Frisch, M. J.; Trucks, G. W.; Schlegel, H. B.; Scuseria, G. E.; Robb, M. A.; Cheeseman, J. R.; Scalmani, G.; Barone, V.; Mennucci, B.; Petersson, G. A.; Nakatsuji, H.; Caricato, M.; Li, X.; Hratchian, H. P.; Izmaylov, A. F.; Bloino, J.; Zheng, G.; Sonnenberg, J. L.; Hada, M.; Ehara, M.; Toyota, K.; Fukuda, R.; Hasegawa, J.; Ishida, M.; Nakajima, T.; Honda, Y.; Kitao, O.; Nakai, H.; Vreven, T.; Montgomery, J., J. A.; Peralta, J. E.; Ogliaro, F.; Bearpark, M.; Heyd, J. J.; Brothers, E.; Kudin, K. N.; Staroverov, V. N.; Kobayashi, R.; Normand, J.; Raghavachari, K.; Rendell, A.; Burant, J. C.; Iyengar, S. S.; Tomasi, J.; Cossi, M.; Rega, N.; Millam, N. J.; Klene, M.; Knox, J. E.; Cross, J. B.; Bakken, V.; Adamo, C.; Jaramillo, J.; Gomperts, R.; Stratmann, R. E.; Yazyev, O.; Austin, A. J.; Cammi, R.; Pomelli, C.; Ochterski, J. W.; Martin, R. L.; Morokuma, K.; Zakrzewski, V. G.; Voth, G. A.; Salvador, P.; Dannenberg, J. J.; Dapprich, S.; Daniels, A. D.; Farkas, Ö.; Foresman, J. B.; Ortiz, J. V.; Cioslowski, J.; Fox, D. J. *Gaussian 09, revision A.02 ed.*; Gaussian Inc.: Wallingford, CT, 2009.
- (61) Peterson, K. A.; Woon, D. E.; Dunning, T., H., Jr. *J. Chem. Phys.* **1994**, *100*, 7410.
- (62) East, A. L. L.; Allen, W. D. *J. Chem. Phys.* **1993**, *99*, 4638.
- (63) Marques, J. M. C.; Prudente, F. V.; Pereira, F. B.; Almeida, M. M.; Maniero, A. M.; Fellows, C. E. *J. Phys. B: At. Mol. Opt. Phys.* **2008**, *41*, 85103.
- (64) Tasic, U.; Yan, T.; Hase, W. L. *J. Phys. Chem. B* **2006**, *110*, 11863.
- (65) Pradeep, T.; Miller, S. A.; Cooks, R. G. *J. Am. Soc. Mass Spectrom.* **1993**, *4*, 769.
- (66) VENUS; VENUS05 is a modified version of VENUS96.
(a) Hase, W. L.; Duchovic, R. J.; Hu, X.; Komornicki, A.; Lim, K. F.; Lu, D.-h.; Peslherbe, G. H.; Swamy, K. N.; Vande Linde, S. R.; Varandas, A.; Wang, H.; Wolf, R. *J. QCPE* **1996**, *16*, 671. (b) Hu, X.; Hase, W. L.; Pirraglia, T. *J. Comput. Chem.* **1991**, *12*, 1014 ed.
- (67) Allen, M. P.; Tildesley, D. J. *Computer Simulation of Liquids*; Clarendon Press: Oxford, 1987.
- (68) Miller, S. A.; Luo, H.; Pachuta, S. J.; Cooks, R. G. *Science* **1997**, *275*, 1447.
- (69) Huang, Y.; Rettner, C. T.; Auerbach, D. J.; Wodtke, A. M. *Science* **2000**, *290*, 111.
- (70) Shenvi, N.; Roy, S.; Tully, J. C. *Science* **2009**, *326*, 829.
- (71) Grimmelmann, E. K.; Tully, J. C.; Cardillo, M. J. *J. Chem. Phys.* **1980**, *72*, 1039.
- (72) Winters, H. F.; Coufal, H.; Rettner, C. T.; Bethune, D. S. *Phys. Rev. B* **1990**, *41*, 6240.
- (73) Martinez-Nunez, E. Unpublished results, 2011.